JOURNAL OF SPACECRAFT AND ROCKETS
Vol. 29, No. 2, March-April 1992

# Viscous Shock-Layer Solutions with Coupled Radiation and Ablation for Earth Entry

Roop N. Gupta*
*NASA Langley Research Center, Hampton, Virginia 23665*
Kam-Pui Lee†
*Vigyan Research Associates, Inc., Hampton, Virginia 23666*
and
James N. Moss* and Kenneth Sutton‡
*NASA Langley Research Center, Hampton, Virginia 23665*

**Results are obtained for the forebody of a planetary exploration vehicle entering the Earth's atmosphere. A viscous shock-layer analysis is used assuming the flow to be laminar and in chemical equilibrium. Presented results include coupled radiation and ablation injection. This study further includes the effect of different transport and thermodynamic properties and radiation models. A Lewis number of 1.4 appears adequate for the radiation-dominated flows. Five velocities corresponding to different possible trajectory points at an altitude of 70 km have been further analyzed in detail. Sublimation and radiative equilibrium wall temperatures are employed for cases with and without coupled injection, respectively. For the cases analyzed here, the mass injection rates are small. However, the rates could become large if a lower altitude is used for aerobraking and/or the body size is increased. A comparison of the equilibrium results with finite-rate chemistry calculation shows the flowfield to be in chemical equilibrium.**

## Nomenclature

$A_{K_{f,i}}, B_{K_{f,i}}, C_{K_{f,i}}, D_{K_{f,i}}, E_{K_{f,i}}$ = curve-fit coefficients for frozen thermal conductivity of species $i$, $K_{f,i}$, Eq. (13)
$A_n$ = coefficients of polynomial curve fits for thermodynamic properties $n = 1, 2, \ldots, 7$, Eqs. (9–11)
$A_{\mu_i}, B_{\mu_i}, C_{\mu_i}$ = curve-fit coefficients for viscosity of species $i$, $\mu_i$, Eq. (12)
$a^*_\infty$ = speed of sound in freestream
$C_i$ = mass fraction of species $i$, $\rho^*_i/\rho^*$
$\tilde{C}_l$ = mass fraction of element $l$, $\sum_i \delta_{il}(M^*_l/M^*_i)\, C_i$
$C_p$ = frozen specific heat of mixture, $\sum_i C_i C_{p,i}$
$C_{p,i}$ = specific heat of species $i$, $C^*_{p,i}/C^*_{p,\infty}$
$\tilde{D}^*$ = self-diffusion coefficient of a reference species
$D^*_{ij}$ = binary diffusion coefficients
$F^{0*}_i$ = free energy of species $i$ at 1 atm (standard state)
$F_i, F_j$ = diffusion factors for species $i$
$h$ = enthalpy of mixture, $\sum_i C_i h_i$
$h^*_a$ = enthalpy of undecomposed ablation material
$h_i$ = enthalpy of species $i$, $h^*_i/U^{*2}_\infty$
$K$ = thermal conductivity of mixture, $K^*/\mu(T^*_{\text{ref}})C^*_{p,\infty}$
$k$ = Boltzmann's constant
$Le$ = Lewis number, $\rho^* D^*_{ij} C^*_p/K^*$
$M^*_i$ = molecular weight of species $i$
$\dot{m}$ = mass injection rate, $\dot{m}^*/\rho^*_\infty U^*_\infty$
$NS$ = total number of species
$n$ = coordinate measured normal to the body, $n^*/R^*_N$
$Pr$ = Prandtl number, $\mu^* C^*_p/K^*$
$p$ = pressure, $p^*/\rho^*_\infty U^{*2}_\infty$
$Q$ = divergence of the net radiative heat flux, $Q^* R^*_N/\rho^*_\infty U^{*3}_\infty$
$q_{\text{cond}}$ = heat flux due to conduction
$q_{\text{conv}}$ = heat flux due to convection
$q_{\text{diff}}$ = heat flux due to diffusion
$q_r$ = net radiative heat flux in $n$ direction, $q^*_r/\rho^*_\infty U^{*3}_\infty$
$q^{(+)*}_r$ = component of radiative flux toward the shock
$q^{(-)*}_r$ = component of radiative flux toward the wall
$-q_{c,w}$ = convective heat flux toward the wall, $-(q_{\text{cond}} + q_{\text{diff}} + q_{\text{conv}})_w$, Eq. (7)
$R^*_{\text{univ}}$ = universal gas constant
$R^*_N$ = nose radius
$r^*$ = radius measured from axis of symmetry to a point on the body surface, Fig. 2
$s$ = coordinate measured along the body surface
$T$ = temperature, $T^*/T^*_{\text{ref}}$
$\bar{T}$ = reduced temperature, $kT^*/\epsilon$
$T^*_{\text{REWT}}$ = radiative equilibrium wall temperature
$T^*_{\text{ref}}$ = references temperature, $U^{*2}_\infty/C^*_{p,\infty}$
$T^*_{\text{sub}}$ = sublimation temperature
$U^*_\infty$ = freestream velocity
$u^*$ = velocity component tangent to body surface, Fig. 2
$v^*$ = velocity component normal to body surface, Fig. 2
$\alpha$ = shock angle defined in Fig. 2
$\Delta H^*_a$ = heat of ablation
$(\Delta h^f_i)^*_{T_{\text{ref}}}$ = standard heat of formation of species $i$ at temperature $T^*_{\text{ref}}$
$\delta_{il}$ = number of atoms of the $l$th element in species $i$
$\delta^*_{\text{sh}}$ = shock standoff distance
$\tilde{\epsilon}$ = Reynolds number parameter, $(\mu^*_{\text{ref}}/\rho^*_\infty R^*_N U^*_\infty)^{1/2}$
$\bar{\epsilon}$ = char emissivity, Eq. (6)
$\epsilon/k$ = potential parameter
$\theta$ = body angle defined in Fig. 2
$\kappa^*$ = body curvature, Fig. 2
$\mu$ = viscosity of mixture, $\mu^*/\mu^*_{\text{ref}}$

Presented as Paper 90-1697 at the AIAA/ASME 5th Joint Thermophysics and Heat Transfer Conference, Seattle, WA, June 18-20, 1990; received June 29, 1990; revision received Sept. 19, 1991; accepted for publication Oct. 21, 1991. 

*Aerospace Technologist, Aerothermodynamics Branch. Associate Fellow AIAA.
†Research Engineer. Member AIAA.
‡Head, Aerothermodynamics Branch. Associate Fellow AIAA.

$\mu^*_{ref}$ = reference viscosity, $\mu^*(T^*_{ref})$
$\rho$ = density of mixture, $\rho^*/\rho^*_\infty$
$\sigma$ = collision diameter
$\sigma^*$ = Stefan-Boltzmann constant
$\Omega^{(1,1)^*}, \Omega^{(2,2)^*}$ = reduced collision integrals

*Subscripts*

$i$ = $i$th species
$l$ = $l$th species
sh = shock value
$w$ = wall value
$-$ = values for the solid ablation material at the surface

*Superscripts*

$\sim$ = values in the shock-oriented coordinate system, Fig. 2
$*$ = dimensional quantity

## Introduction

THERE is a recent revival of interest in both manned and unmanned exploration of our solar system. The focus of this increased interest is planet Mars[1] because of its striking similarity to Earth. To minimize the weight of space exploration vehicles, aerobraking (using aerodynamic drag to produce the desired velocity change) has been suggested[2,3] as an effective alternative to an all-propulsive system for atmospheric insertion both at Mars and on return to Earth. This paper is related to the problems encountered during the high-energy entry into the Earth's atmosphere.

The flowfield surrounding a planetary exploration vehicle can be quite complex because of the presence of ablative products (from the heat shield) in the flow and its coupling with the radiative transport. Under the high-energy entry conditions, there is a strong interaction between the flowfield and the heat-shield material. This may result in large ablation rates. Since simulation of the high-energy thermodynamic environment of planetary entries in ground-based experimental facilities is difficult, accurate and reliable flowfield prediction capabilities must be developed for efficient and reliable design of planetary vehicles.

References 4–7 have analyzed stagnation-region flows about planetary probes. Sutton[8] and Moss[9] have presented stagnation-region and downstream solutions for viscous radiating flows. Sutton's approach[8] involves coupling a boundary-layer solution with an inviscid shock-layer solution. Moss,[9] employing the viscous shock-layer (VSL) equations, obtained results for coupled radiative ablation injection. The VSL analysis of Moss[9,10] has been extensively used to provide detailed flowfield calculations for the outer planetary probes,[11,12] including the "benchmark" calculations for the design of the Galileo probe.[13]

Park and Milos[14] recently presented results for the one-dimensional inviscid flow through a diverging nozzle using the vibrational temperature to obtain the radiative properties. These results have been computed by employing a time-asymptotic method, which oscillates through its convergence history and is very time inefficient. Observations by Park and Milos[14] about the VSL method of Refs. 9, 10, 13, and 15 are misleading. First, there are no convergence problems for the low-to-moderate surface injection rates. The VSL method of Refs. 9, 10, and 13 has recently been updated[16] by coupling the normal momentum and continuity equations, which makes the method of Refs. 9, 10, and 13 stable even for the massive blowing conditions. Next, even though the radiation is computed explicitly, it is fully coupled to the flowfield equations through a locally iterative procedure under the so-called tangent-slab approximation. The explicitly coupled radiation computation approach used in the VSL method (with updating of the computed radiation through local iterations) appears physically consistent and gives oscillation-free and computationally efficient results.

In this study, we present results from a viscous shock-layer analysis for the high-energy flowfields under chemical equilibrium for Earth entry conditions. This analysis is based on the work or Refs. 9 and 10. The focus of the present calculations is the flowfield around bodies (with carbon-phenolic heat shields) for Earth-return aerobraking in the range of 12–16 km/s and altitudes of about 70 km or less (see Fig. 1). Under these entry conditions, large gradients (particularly temperature) are obtained behind the shock because of the large radiation cooling. Consequently, the transport effects should not be neglected in this region. Furthermore, the flowfield gradients behind the shock must be resolved finely for an accurate estimate of the surface radiative heating. A viscous shock-layer model is a very practical and efficient means of calculating such flows.

The results presented here include the sensitivity of the heating to transport and thermodynamic properties and radiation models. Results are obtained by employing both the radiative equilibrium wall temperature (for no ablation injection cases) and the sublimation temperature (for the coupled ablation injection cases). The effect of coupled carbon-phenolic injection on the stagnation and downstream heating is analyzed. Finally, an estimate of the effect of finite-rate flowfield chemistry on various flowfield quantities is included for the case of no injection and no radiation.

## Analysis

### Flowfield Model

The physical model and the coordinate system for an Earth entry body are shown in Fig. 2. The flow in the shock layer is assumed to be axisymmetric, steady, laminar, viscous, and compressible. The viscous shock-layer equations for such a multicomponent radiating gas mixture under chemical equilibrium conditions are presented in Ref. 9 in the body-oriented coordinate system of Fig. 2. The governing equations for the present study are the same as those of Ref. 9 and, therefore, are not given here. The present analysis provides for ablation injection at the surface and includes a detailed description of the radiative transport, equilibrium chemistry, and thermody-

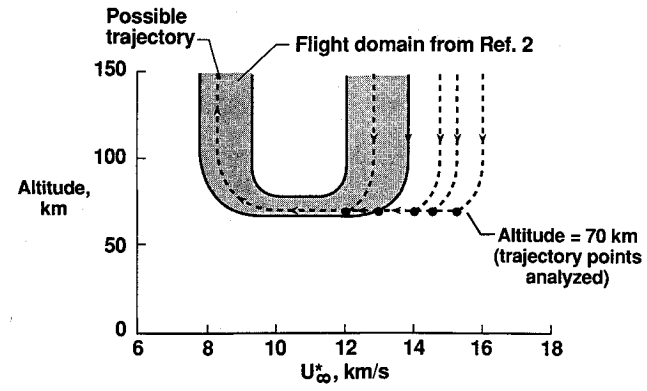


Fig. 1 Trajectory points analyzed for Earth aerobraking.

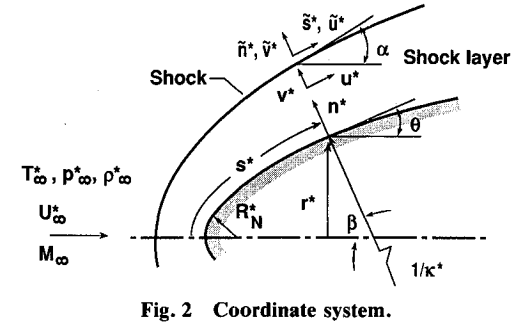


Fig. 2 Coordinate system.

namic and transport properties. Results for the finite-rate chemistry with no injection and flowfield radiation are based on the method of Ref. 16 with the details of chemical kinetics provided in Refs. 10 and 17.

**Boundary Conditions**

The boundary conditions at the shock are obtained by using the Rankine-Hugoniot relations. No-slip and no-temperature-jump boundary conditions are used at the body surface. The wall temperature and injection rate are either specified or calculated. For the calculated conditions, the mass injection rate is obtained from an energy balance at the flowfield-ablator interface. The expression for the coupled mass injection rate for steady-state ablation is

$$\dot{m} = \left( \frac{-q^*_{c,w} - q^*_{r,w}}{\sum_{i=1}^{NS} (C_i h^*_i)_w - h^*_a} \right) \Bigg/ (\rho^*_\infty U^*_\infty) \tag{1a}$$

or

$$= \left( \frac{-q^*_{c,w} - q^*_{r,w}}{\Delta H^*_a} \right) \Bigg/ (\rho^*_\infty U^*_\infty) \tag{1b}$$

Furthermore, the surface temperature for the coupled ablation calculations was specified by assuming quasisteady sublimation. The expressions used for the sublimation temperature and the heat of ablation for a carbon-phenolic ablator are

$$T^*_{\text{sub}} = 3736.0 + 306.0 \log p^* + 26.0 (\log p^*)^2, \text{ K} \tag{2}$$

$$\Delta H^*_a = 24.9 - 1.8 \log p^* + 1.1 (\log p^*)^2, \text{ MJ/kg} \tag{3}$$

where $p^*$ is the wall pressure in atmosphere. These equations are applicable for surface pressures of 0.01–10.0 atm and for the condition where the gas species adjacent to the surface are due solely to the ablation species. The surface temperature and the coupled mass injection rate are calculated by iterating the solution of the governing flowfield equations and the boundary conditions.

For ablation injection, the elemental concentrations at the wall are governed by convection and diffusion and are obtained from the equation

$$\left( \frac{\partial \tilde{C}_l}{\partial n} \right)_w - \frac{1}{\tilde{\epsilon}^2} \left( \frac{\dot{m} Pr}{\mu Le} \right)_w [(\tilde{C}_l)_w - (\tilde{C}_l)_-] = 0 \tag{4}$$

For the radiative transport calculations, the bow shock is considered transparent and the freestream is considered cold and transparent. Therefore, the precursor effects are neglected. Further, the body surface is assumed to be gray with a reflective of 0.1, emissivity of 0.9, and transmissivity of 0. The energy reradiated from the surface is included both in the radiation transport calculation as well as in the surface energy balance [Eqs. (1)]. The net radiative flux can be represented as

$$q_r = q_r^{(+)} - q_r^{(-)} \tag{5}$$

At the surface

$$q^{(+)^*}_{r,w} = \bar{\epsilon} \sigma^* T^{*4}_w \tag{6}$$

The heat transferred to the wall because of conduction, diffusion, and convection is

$$-q_{c,w} = \tilde{\epsilon}^2 \left[ K \frac{\partial T}{\partial n} + \frac{\mu Le}{Pr} \sum_{i=1}^{NS} h_i \frac{\partial C_i}{\partial n} - \dot{m} \sum_{i=1}^{NS} (C_i h_i - C_{i-} h_{i-}) \right]_w \tag{7}$$

For some of the cases analyzed here ($U^*_\infty < 13.6$ km/s, $R^*_N = 3.05$ m, and alt = 70 km), the surface heating was insufficient to produce sublimation. That is, the radiative heat flux emitted from the surface at the sublimation temperature exceeded the heat flux incident upon the surface. For these cases, the surface temperature is assumed to be the radiative equilibrium wall value as given by

$$T^*_{\text{REWT}} = \left\{ \left[ q_r^{(-)} - \tilde{\epsilon}^2 \left( K \frac{\partial T}{\partial n} + \frac{\mu Le}{Pr} \sum_{i=1}^{NS} h_i \frac{\partial C_i}{\partial n} \right) \right] \frac{\rho^*_\infty U^{*3}_\infty}{\bar{\epsilon} \sigma^*} \right\}^{1/4} \tag{8}$$

**Radiative Transport**

The radiative flux $q_r$ and the divergence of the radiative flux $Q$ are calculated with the radiation transport code RADICAL.[18,19] This code accounts for the effects of nongray self-absorption. Molecular-band, continuum, and atomic-line transitions are included. A detailed frequency dependence of the absorption coefficient is used for integrating over the radiation frequency spectrum, and the tangent-slab approximation is used for integrating over physical space. The chemical species considered in the present study of determining the radiative transport are O, $O_2$, $O^+$, $O^-$, N, $N_2$, $N^+$, $N^-$, $N_2^+$, $e^-$, NO, C, $C_2$, $C_3$, $C^+$, $C^-$, CO, CN, H, $H_2$, and $H^-$. The radiation code automatically obtains the mole fraction of the species $N_2^+$, $N^-$, $O^-$, $C^-$, and $H^-$ from Saha's equation.[20] The ultraviolet radiation properties used here for $C_3$ are those of Ref. 21.

**Thermodynamic and Transport Properties**

The equilibrium composition is determined by a free-energy minimization calculation as developed in Ref. 22. Thermodynamic properties of specific heat, enthalpy, and free-energy and transport properties for viscosity and thermal conductivity are required for each species considered. Values for the thermodynamic and transport properties for the air species are obtained from the polynomial curve fits of Ref. 23. Thermodynamic properties for the ablation products are obtained by using the polynomial curve-fit constants of Table 1 given in Ref. 24 in the following equations:

Specific heat:

$$\frac{C^*_{p,i}}{R^*_{\text{univ}}} = A_1 + A_2 T^* + A_3 T^{*2} + A_4 T^{*3} + A_5 T^{*4} \tag{9}$$

Specific enthalpy:

$$\frac{h^*_i}{R^*_{\text{univ}} T^*} = A_1 + \frac{A_2 T^*}{2} + \frac{A_3 T^{*2}}{3} + \frac{A_4 T^{*3}}{4} + \frac{A_5 T^{*4}}{5} + \frac{A_6}{T^*} \tag{10}$$

Free energy:

$$\frac{F^{0*}_i}{R^*_{\text{univ}} T} = A_1 [1 - \ell n(T^*)] - \frac{A_2 T^*}{2} - \frac{A_3 T^{*2}}{6} - \frac{A_4 T^{*3}}{12} - \frac{A_5 T^{*4}}{20} + \frac{A_6}{T^*} - A_7 \tag{11}$$

The various polynomial coefficients of Eqs. (9–11) have been evaluated by using the least-squares curve-fit technique. The polynomial coefficients for C, $C_2$, $C_3$, CO, CN, and $C^+$ have been evaluated by curve fitting the tabulated values of thermodynamic properties given by Browne[25,26]; coefficients for H, $H_2$, $C_2H$, and $C_2H_2$ are obtained by curve fitting the tabulated properties of Ref. 27; coefficients for HCN are obtained from the curve fit to the tabulated values of Ref. 28; and coefficients for $C_3H$ and $C_4H$ are obtained from the tabulated values of Ref. 29. Heats of formation for various substances from Refs. 25–29 are given in Table 2 of Ref. 24.

The transport properties (i.e., viscosity and frozen thermal conductivity) for the carbon-phenolic ablation products are obtained from the following equations:

$$\mu^*_i = (e^{C_{\mu_i}}) T^{*[A_{\mu_i} \ell n T^* + B_{\mu_i}]} \tag{12}$$

$$K^*_{f,i} = (e^{E_{K_{f,i}}})T^{*[A_{K_{f,i}}(\ell nT^*)^3 + B_{K_{f,i}}(\ell nT^*)^2 + C_{K_{f,i}}(\ell nT^*) + D_{K_{f,i}}]} \quad (13)$$

With the exception of five species (H, $H_2$, C, $C^+$, and CO), the coefficients appearing in these equations (provided in Tables 3 and 4 of Ref. 24) have been obtained by curve fitting the computed values from the following expressions:

$$\mu^*_i = \frac{2.6693 \times 10^{-5} M_i T^*}{\sigma^2 \Omega^{(2,2)^*}} \quad (14)$$

$$K^*_{f,i} = K^*_{\mathrm{tr},i} + K^*_{\mathrm{int},i} \quad (15a)$$

$$K^*_{\mathrm{tr},i} = \frac{1.9891 \times 10^{-4} M_i T^*}{\sigma^2 \Omega^{(2,2)^*}} \quad (15b)$$

$$K^*_{\mathrm{int},i} = 6.3605 \times 10^{-5} \frac{T^*/M_i}{\sigma^2 \Omega^{(1,1)^*}} \quad (15c)$$

where $\Omega^{(1,1)^*}$ and $\Omega^{(2,2)^*}$ are the reduced collision integrals (which are a function of the reduced temperature, $\bar{T} = kT^*/\epsilon$). The values used for these collision integrals were those for the Lennard-Jones (6-12) potential that are tabulated in Ref. 30 as a function of the reduced temperature $\bar{T}$. The force constants $\sigma$ and $\epsilon/k$ are taken from Svehla.[31]

Caution should be exercised in evaluating the thermal conductivity $K^*_{f,i}$ from the coefficients given in Table 4 of Ref. 24. All of the five significant digits for the coefficients should be used. Further, the thermal conductivity should be evaluated from the logarithmic form of Eq. (13):

$$\ell nK^*_{f,i} = A_{K_{f,i}} Z^4 + B_{K_{f,i}} Z^3 + C_{K_{f,i}} Z^2 + D_{K_{f,i}} Z + E_{K_{f,i}} \quad (16a)$$

with

$$Z = \ell nT^* \quad (16b)$$

for reasons of accuracy because the exponent of the exponential term (namely, $E_{K_{f,i}}$) in Eq. (13) is a large number.

Values for the five species H, $H_2$, C, $C^+$, and CO are tabulated in an unpublished work of Yos.[32] The coefficients for these five species have been obtained by curve fitting those tabulated values.

Mixture viscosity is obtained by the method of Armaly and Sutton,[33] and mixture thermal conductivity is computed by the Mason and Saxena[34] relation. A variable Prandtl number along with either a constant or a variable Lewis number is used. A value of 1.4 is used for the constant Lewis number calculation, and a binary diffusion approximation is used for computing the variable Lewis number. The binary diffusion coefficient is set equal to that for atomic carbon diffusing into atomic nitrogen for the case of carbon-phenolic injection. For no injection or air injection into air, the binary diffusion coefficient is assumed to be that for molecular nitrogen diffusing into atomic oxygen.

Air is treated as a mixture of nine chemical species: O, $O_2$, $O^+$, N, $N_2$, $N^+$, NO, $NO^+$, and $e^-$. For ablation injection, 20 chemical species are used: the seven air species (without NO and $NO^+$) plus C, $C_2$, $C_3$, CO, CN, $C_2H$, $C_3H$, $C_4H$, $C_2H_2$, $C^+$, H, $H_2$, and HCN.

## Method of Solution

Moss presented a method[10] for solving the viscous shock-layer equations for reacting multicomponent mixtures for stagnation and downstream flow. Present results for the equilibrium flow chemistry have been obtained by the method of solution that is identical to that of Ref. 10 and, therefore, is not presented here. Similarly, the results for finite-rate chemistry, no ablation injection, and no radiation are computed by the method of Refs. 16 and 17. Hence, the details of this method are not provided here either.

## Results and Discussion

This study presents results for specified and coupled mass injection rates with equilibrium flowfield chemistry for high-energy entry into the Earth's atmosphere. The injectants considered are either air or carbon-phenolic ablation species.

### Comparison with Existing Numerical Results

First, an evaluation of the present predictions is made by comparison with the numerical predictions of Refs. 7-9. Each of these three references has presented stagnation results for the following Earth entry conditions: alt = 60.96 km, $U^*_\infty$ = 15.24 km/s, $R^*_N$ = 3.05 m, and $T^*_w$ = 3600 K. For these calculations, the freestream Reynolds number is $0.78 \times 10^6$, and the shock temperature and pressures are 14,650 K and 0.59 atm, respectively. The surface mass injection rates are specified, and the ablator elemental mass fractions are 0.049 oxygen, 0.009 nitrogen, 0.920 carbon, and 0.022 hydrogen.

Figure 3 shows a comparison of the present results with those of Moss[9] for the wall heat fluxes. The results are for carbon-phenolic injection with mass injection rates $\dot{m}$, varying from 0 to 0.4. The two predictions for the radiative heat flux (shown in Fig. 3a) are in fairly good agreement considering the differences in the transport and thermodynamic properties and the radiation models used in the two calculations. The present results have been obtained from the radiation model of Nicolet[18,19] by using the transport and thermodynamic properties for the C-H-N-O system from Ref. 23 and those presented in Tables 1-4 of Ref. 24. Results from Ref. 9 were obtained by employing the radiation model and the transport and thermodynamic properties from Refs. 35 and 36.

The conductive and diffusive wall heat fluxes from the present calculations and those of Ref. 9 are compared in Fig. 3b. The differences in the two results are large for the

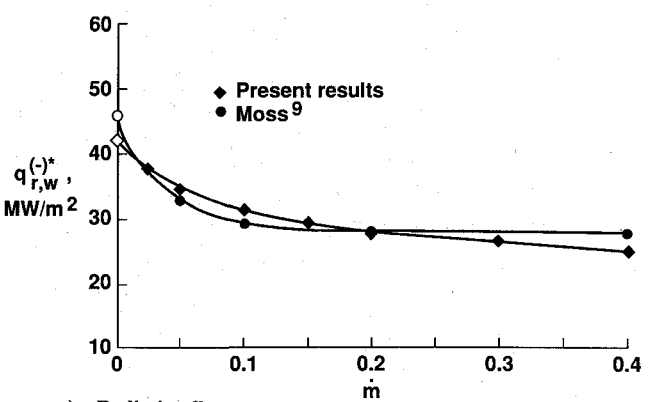


a) Radiative flux

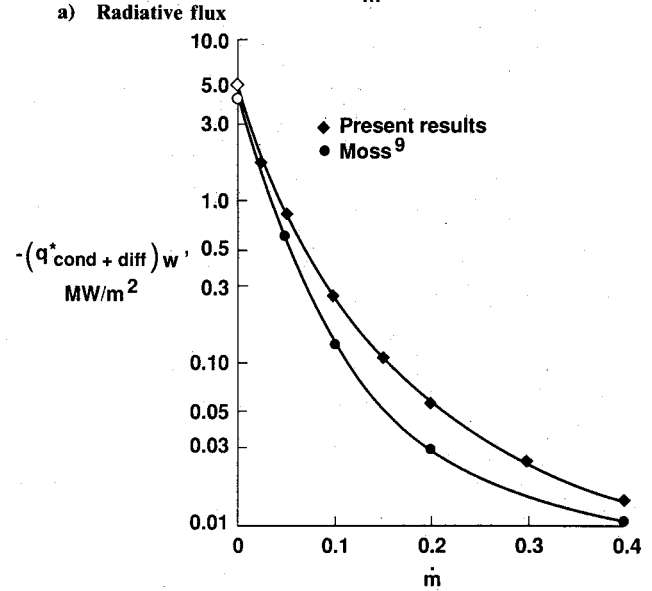


b) Conductive plus diffusive fluxes

**Fig. 3 Comparison of stagnation-point heat fluxes (alt = 60.96 km, $R^*_N$ = 3.05 m, $U^*_\infty$ = 15.24 km/s, $T^*_w$ = 3600 K).**

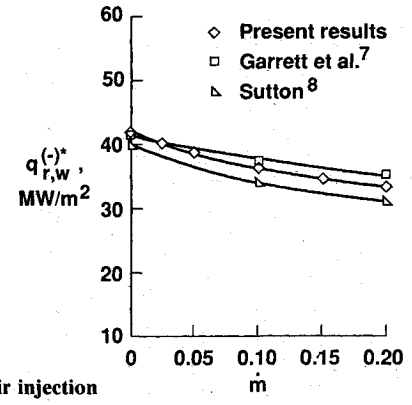


a) Air injection

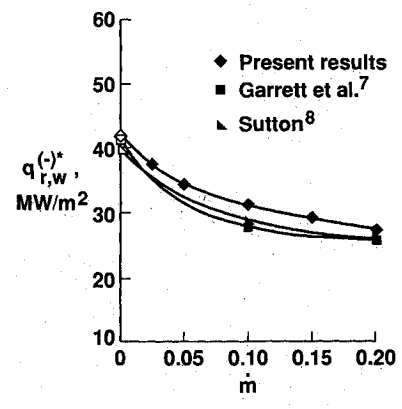


b) Carbon-phenolic injection

**Fig. 4 Comparison of stagnation-point radiative heat fluxes with mass (alt = 60.96 km, $R_N^* = 3.05$ m, $U_\infty^* = 15.24$ km/s, $T_w^* = 3600$ K).**

larger values of the mass injection parameter $\dot{m}$. This appears to be because of the difference in the transport and thermodynamic properties, especially those of the ablation products used in the two calculations.

Figures 4a and 4b show comparison of the present radiative heat flux results with those of Refs. 7 and 8 for air and carbon-phenolic injections, respectively. The present results shown in Fig. 4a are obtained with Nicolet's radiation model,[18,19] and the transport and thermodynamic properties are from Gupta et al.[23] The present results shown in Fig. 4b are the same as those given in Fig. 3a. The results presented in Figs. 4a and 4b are in reasonable agreement considering the differences in details of the analyses, solution procedures, radiation models, and transport and thermodynamic properties.

### Effects of Flowfield Properties and Radiation Models on Radiative Heating

This section discusses the effect of employing different thermodynamic and transport properties and different radiation models.

*Effect of Transport and Thermodynamic Properties of Air*

For air injection, Fig. 5 shows that the wall radiative heat flux predictions using the thermodynamic and transport properties of Ref. 23 are lower by about 10–20% as compared with those obtained with the properties of Ref. 36. The radiation model used with these predictions is that of Ref. 18.

*Effect of Transport and Thermodynamic Properties of Ablation Products*

Figure 6 shows the effect of using the thermodynamic and transport properties from Tables 1–4 given in Ref. 24 and those of Ref. 36 on radiative heat flux (with carbon-phenolic injection). The present values for the properties give higher radiative flux with a maximum difference of about 4% at $\dot{m} = 0.4$.

*Effect of Variable Lewis Number*

Results have been obtained here for both variable and constant Lewis number values. For the variable Lewis number calculations, a binary diffusion model is used. The binary diffusion coefficients for these calculations are computed on the basis of the dominant species present. With carbon-phenolic injection, the dominant species are atomic carbon for the ablator and atomic nitrogen for air; hence, the binary diffusion coefficient for diffusion of atomic carbon and atomic nitrogen has been used in the computations. This assumption is found to be valid[7] for the conditions analyzed here. Similarly, for no injection or injection with air, the binary diffusion coefficient for diffusion of molecular nitrogen and atomic oxygen is used.

Figure 7a shows that the effect of using a variable Lewis number on wall radiative flux is negligible. This is understandable because the Lewis number should affect more strongly those processes that involve diffusion directly as shown in Fig. 7b. The three components of the wall convective heat flux (conduction, diffusion, and convection), as given by Eq. (7), are sensitive to the way in which the Lewis number is evaluated. Except for the no-injection case ($\dot{m} = 0$), the variable Lewis number gives lower values for the wall convective heat fluxes than the constant Lewis number values. As seen from Figs. 7a and 7b, radiation is the dominant mode of heat transfer for the conditions analyzed, and the role played by Lewis number in impacting the overall surface heating becomes secondary.

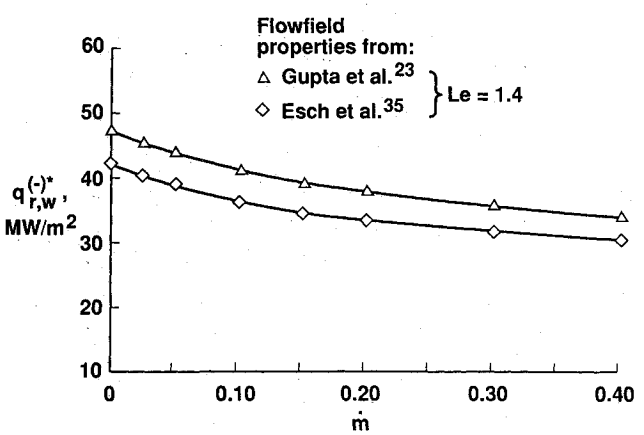


**Fig. 5 Comparison of stagnation-point radiative heat fluxes with different flowfield properties for air injection; radiation model is from Nicolet[18] (alt = 60.96 km, $R_N^* = 3.05$ m, $U_\infty^* = 15.24$ km/s, $T_w^* = 3600$ K).**

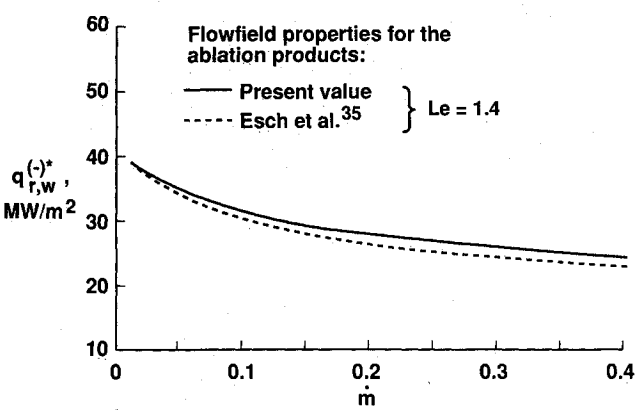


**Fig. 6 Comparison of stagnation-point radiative heat fluxes with carbon-phenolic injection; flowfield properties for the air species are from Gupta et al.[23] (alt = 60.96 km, $R_N^* = 3.05$ m, $U_\infty^* = 15.24$ km/s, $T_w^* = 3600$ K).**

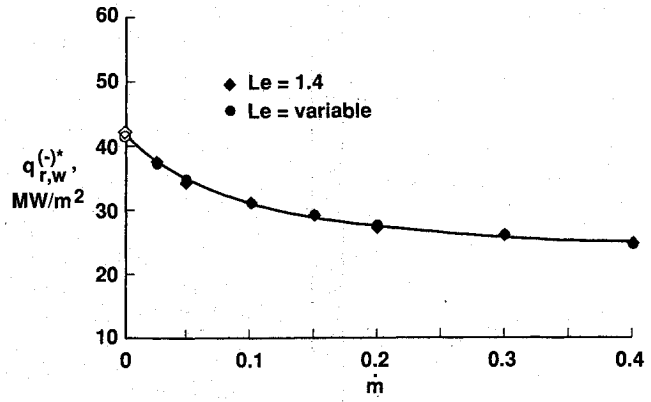


a) Radiative flux

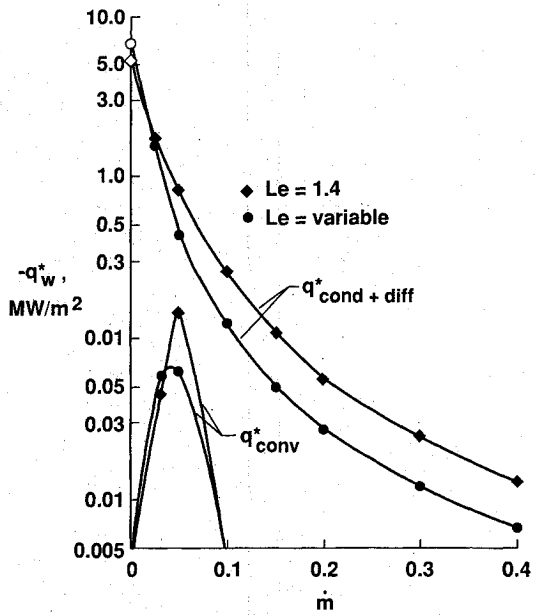


b) Convective and conduction plus diffusion fluxes

**Fig. 7 Effect of Lewis number on stagnation-point heat fluxes (alt = 60.96 km, $R^*_N = 3.05$ m, $U^*_\infty = 15.24$ km/s, $T^*_w = 3600$ K).**

*Effect of Radiation Models (with Air Injection)*

The effect of using two different radiation models (those of Refs. 18 and 35) is shown in Fig. 8 by employing the same flowfield properties for the two calculations from Ref. 36. The present results (obtained by employing the radiation model of Ref. 18) are comparable with the calculation of Moss (which used the radiation model of Ref. 35) for values of $\dot{m}$ less than 0.1. The differences between the two predictions, however, increase for $\dot{m} > 0.1$ with the maximum differences of about 10% at $\dot{m} = 0.4$.

**Calculations for Earth Entry at 70-km Altitude**

*Chemical Equilibrium*

After validating the present code with other predictions and verifying the effect of various flowfield quantities on surface heat transfer, results are now presented for the five velocities corresponding to different trajectories shown in Fig. 1 at an altitude of 70 km. The freestream conditions and selected stagnation point results for these trajectory points are provided in Table 1. This table includes results for the shock standoff distance and surface convective heating with and without radiation in the flowfield calculations. With radiation cooling, the shock standoff distance is smaller due to the lower temperature (and higher densities) in the shock layer than the case without radiation.

Results for the condition of Table 1 have been obtained with radiative equilibrium wall temperatures for no surface injection (i.e., $\dot{m} = 0$) and with sublimation wall temperatures for coupled ablation injection. These temperatures for the five trajectory points are given in Fig. 9. One may notice from this figure that, for a freestream velocity less than about 13.6 km/s, the surface heating is insufficient to cause sublimation (for 70-km altitude, $R^*_N = 3.05$ m, and a carbon-phenolic ablator). The coupled ablation injection results, therefore, could not be computed for $U^*_\infty = 13.6$ km/s. Figure 9 serves to provide the maximum wall temperature one may expect for the five trajectory points. For $U^*_\infty = 13.6$ km/s, the maximum temperatures would lie below the radiative equilibrium curve, whereas for $U^*_\infty = 13.6$ km/s the maximum possible temperatures are those corresponding to the respective sublimation value.

Figure 10 gives the stagnation-point heat fluxes corresponding to the surface temperatures of Fig. 9 for the five trajectory points. The freestream Reynolds numbers, shock temperatures, and shock pressures along with other flowfield quantities are given in Table 1. The radiative heat flux is dominant

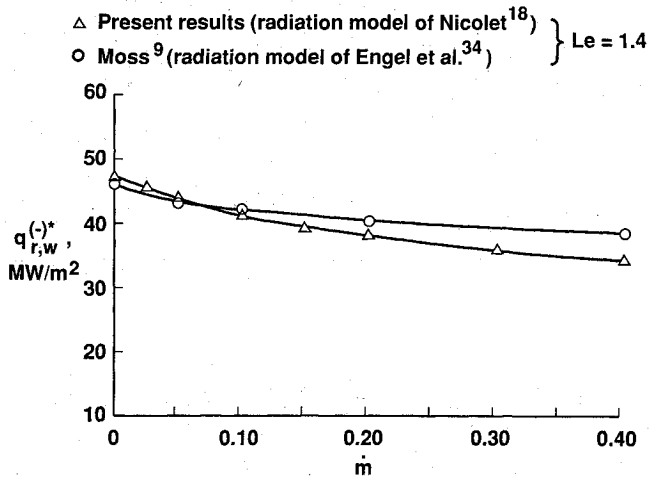


**Fig. 8 Comparison of stagnation-point radiative heat fluxes with different radiation models for air injection; flowfield properties are from Esch et al.[36] (alt = 60.96 km, $R^*_N = 3.05$ m, $U^*_\infty = 15.24$ km/s, $T^*_w = 3600$ K).**

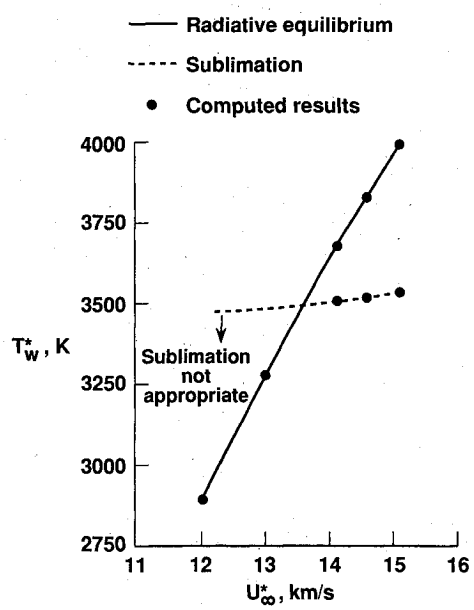


**Fig. 9 Stagnation-point sublimation and radiative equilibrium wall temperatures with and without coupled ablation injection, respectively (alt = 60.96 km, $R^*_N = 3.05$ m).**

**Table 1 Freestream conditions and selected stagnation point results for no injection[a]**

| $U^*_\infty$, km/s | $Re_{\infty,R^*_N}$ | $p^*_{sh}$, atm | $\rho^*_{sh}/\rho^*_\infty$ | $T^*_{sh}$, K | $T^*_{REWT}$,[b] K | $q^{(-)^*}_{r,w}$ MW, m² | $\delta^*_{sh}$, cm | | $-q^*_{c,w}$, MW/m² | |
|---|---|---|---|---|---|---|---|---|---|---|
| | | | | | | | With radiation | Without radiation | With radiation | Without radiation |
| 12.00 | $0.22 \times 10^6$ | 0.12 | 17.14 | 11,360 | 2,880 | 2.35 | 12.66 | 13.57 | 1.46 | 1.33 |
| 13.00 | $0.24 \times 10^6$ | 0.14 | 17.53 | 12,060 | 3,245 | 4.20 | 11.98 | 13.31 | 1.87 | 1.57 |
| 14.00 | $0.26 \times 10^6$ | 0.16 | 17.87 | 12,720 | 3,620 | 6.96 | 11.30 | 13.11 | 2.29 | 1.81 |
| 14.50 | $0.27 \times 10^6$ | 0.17 | 17.94 | 13,050 | 3,760 | 8.48 | 11.00 | 13.05 | 2.55 | 1.97 |
| 15.24 | $0.28 \times 10^6$ | 0.19 | 18.08 | 13,560 | 3,990 | 11.05 | 10.56 | 13.00 | 2.96 | 2.14 |

[a]Alt = 70 km, $\rho_\infty = 8.75 \times 10^{-5}$ kg/m³, $R^*_N = 3.05$ m, $T^*_\infty = 220$ K, $a^*_\infty = 297.14$ m/s.
[b]Obtained from surface heating with radiation; same value used for cases without radiation.

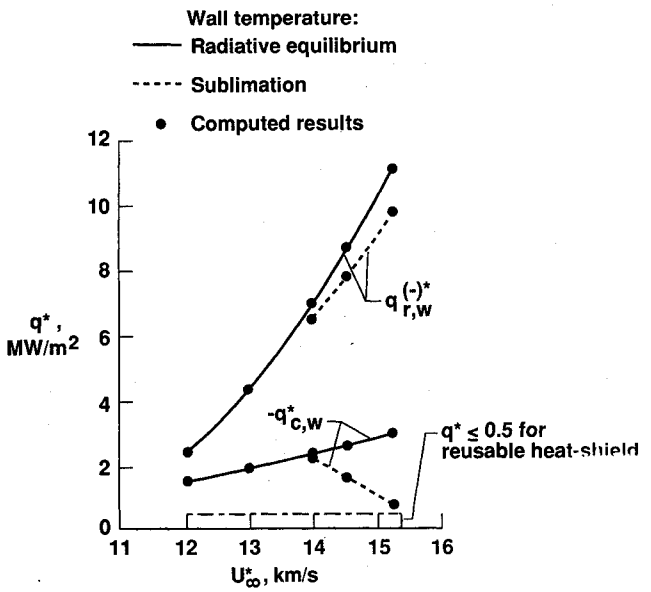


**Fig. 10 Stagnation-point heat fluxes for different Earth entry velocities with and without coupled ablation injection (alt = 70 km, $R^*_N = 3.05$ m).**

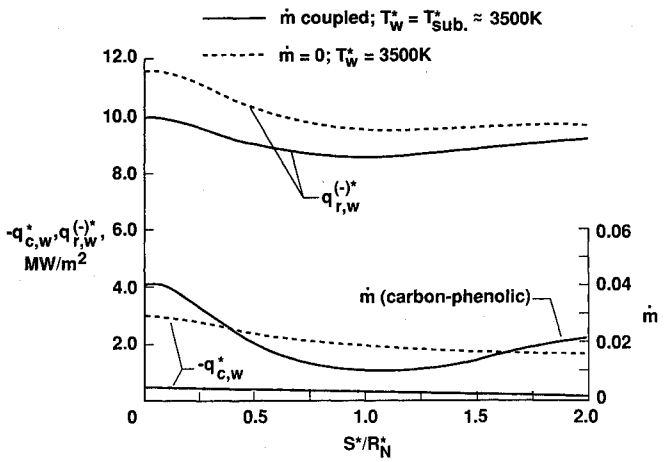


**Fig. 11 Distribution of surface quantities for a 60-deg half-angle hyperboloid with and without coupled injection (alt = 70 km, $R^*_N = 3.05$ m, $U^*_\infty = 15.24$ km/s).**

for all cases. For the lower velocity cases where no ablation injection is considered (even though ablation products would be present but the assumption of sublimation would be inappropriate), the radiative and convective heat fluxes become comparable. [For flow conditions where the surface heating is insufficient to support sublimation yet greater than that for pyrolysis, ablation products (pyrolysis and char removal due to oxidation)[37,38] would still be injected into the flowfield and would produce surface temperatures that are less than those calculated for the radiative equilibrium assumption.] For the coupled stagnation results, the calculated injection rates are small with $\dot{m} = 0.009$, 0.019, and 0.041 for $U^*_\infty = 14$, 14.5, and 15.24 km/s, respectively. Consequently, the reduction in radiative heating is also relatively small, even though the convective heating and the surface temperatures (compared with the radiative equilibrium wall value) are reduced considerably.

The stagnation-point heating rate values shown in Fig. 10 indicate that a vehicle with a nose radius smaller than 3.05 m would produce a reduction in combined convective and radiative heating for the higher velocity conditions. For velocities near 12 km/s, the current nose radius is close to an optimal size for achieving a minimum heating rate. Furthermore, since a reusable heat shield[39] is not generally feasible (with the currently available material for a heat rate above 0.5 MW/m²), vehicles experiencing the flight conditions analyzed here will require an ablative thermal protection system.

Figure 11 shows the wall heat fluxes with and without coupled ablation injection along a 60-deg half-angle hyperboloid body. Also shown is the coupled mass injection distribution. For this case, the freestream velocity was 15.24 km/s, the freestream Reynolds numbers was $0.28 \times 10^6$, and the stagnation shock temperature and pressure were 13,560 K and 0.19 atm, respectively. Other freestream conditions are given in Table 1. The sublimation temperature resulting from the coupled injection calculation is almost constant along the body surface (within 1% of the stagnation-point value of 3500 K). For the 60-deg hyperboloid body shape considered, the shock-layer thickness increases substantially with distance downstream from the stagnation point. Consequently, the radiative heating and mass injection do not continue to decrease with increasing distance downstream. For the case analyzed here, the convective heating with injection is negligible compared with the radiative component because of the mass injection along the entire length of the body.

To evaluate the effects of surface injection, calculated results for no injection and $T^*_w = 3500$ K are also shown in Fig. 11. The stagnation point radiative heat flux is reduced by 10% and the convective heat flux is reduced by 83% with coupled injection. However, the overall heat flux is not reduced substantially because of the relatively small reduction in the radiative component of the total heat flux. The radiative component dominates heating in this case. Results of Fig. 11 could change, however, if the altitude is lowered and/or the body nose radius is increased. Both of these changes could result in massive surface ablation.

For the coupled ablation injection rates obtained with the calculations presented in Figs. 10 and 11, the gas composition adjacent to the surface is due to both ablation and air species. Curve fits of Eqs. (2) and (3), however, assume that the gas species adjacent to the surface are due solely to the ablation species. This is true only for massive injection. These curve fits, therefore, need to be modified (similar to Ref. 13) to account for the situation when the gas composition adjacent to the surface is not due solely to the ablation species.

*Chemical Nonequilibrium Effects*

Figures 12 and 13 characterize the nature of the flowfield chemistry. The results contained in Figs. 3–12 are under the

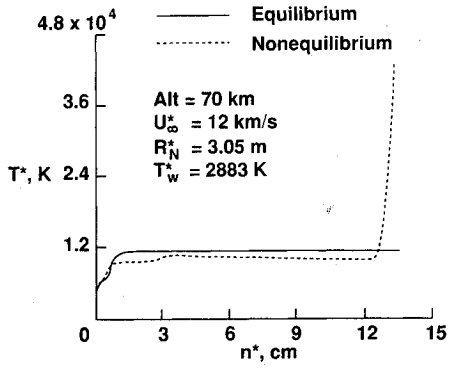


**Fig. 12 Temperature profiles at the stagnation point with equilibrium and nonequilibrium flowfield chemistry.**

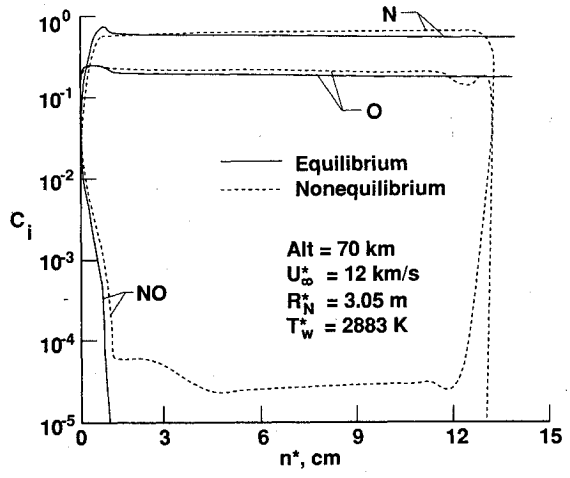


**Fig. 13 Concentration profiles at the stagnation point with equilibrium and nonequilibrium flowfield chemistry.**

assumption of chemical equilibrium. To evaluate this assumption the trajectory point of Fig. 1 at $U_\infty^* = 12$ km/s (the lowest Reynolds number case) has been further analyzed by repeating the calculation with a finite-rate chemistry calculation. [If the lowest Reynolds number case (corresponding to the lowest velocity of 12 km/s considered here) happens to be in chemical equilibrium, then higher velocity cases (with higher values of the Reynolds number, see Table 1) are going to be in equilibrium too. High Reynolds number flows are essentially equilibrium chemistry flows and are typified by the existence of a thin viscous boundary layer close to the surface followed by a large inviscid shock layer as seen Fig. 12.] For the nonequilibrium chemistry calculation, the wall boundary condition for the chemical species was the same as that for the equilibrium chemistry calculation. A comparison between the stagnation temperature profiles obtained from the equilibrium and finite-rate chemistry VSL calculations (Fig. 12) clearly shows that the flowfield is in chemical equilibrium. A small viscous boundary layer (less then 20% of the shock-layer thickness) is followed by the large inviscid shock layer, which is characteristic of high Reynolds number, equilibrium chemistry flows. With the finite-rate chemistry calculations, the temperature behind the shock quickly (in less than about 6% of the shock-layer-thickness distance) relaxes from the frozen-flow value across the shock to approximately the equilibrium-flow value. The flow is assumed frozen at the freestream composition for the shock crossing in the finite-rate chemistry calculations. The finite-rate results take much longer to converge when the flowfield chemistry approaches equilibrium. In fact, the present finite-rate results are not fully converged in that the sum of the elemental composition exceeds unity in the vicinity of the boundary-layer edge. The maximum error for the results presented was 7%, and the rate of convergence was extremely slow when the computation was terminated. This convergence problem encountered in the calculation of flows near chemical equilibrium by a finite-rate procedure is similar to that of previous experience and requires additional study. With fairly high temperatures behind the shock, the flow rapidly dissociates, ionizes, and approaches the equilibrium composition as shown in Fig. 13.

## Concluding Remarks

Results are presented for the forebody of a planetary exploration vehicle entering the Earth's atmosphere. Solutions are obtained with a viscous shock-layer (VSL) analysis where the flow is assumed to be laminar and in chemical equilibrium. Results presented include coupled radiation and ablation injection. Recently developed curve fits are used for the transport and thermodynamic properties for the air species and ablation products. A detailed comparison with existing results is provided to evaluate the effect of two radiation models and transport and thermodynamic properties. Since most of the cases analyzed here are dominated by radiative heating, variable Lewis number does not impact the overall surface heating substantially. A constant Lewis number of 1.4 appears adequate for the cases considered.

Detailed results for five entry velocities at an altitude of 70 km are analyzed for the possible heating conditions that may be encountered by the proposed planetary exploration vehicles. Results are obtained both with and without coupled injection using the sublimation and radiative-equilibrium wall temperatures, respectively. These are the maximum temperatures one would encounter for the conditions analyzed here. The corresponding heat flux values show that the overall surface heating reduction with coupled ablation injection (from that of the nonablating VSL results) is modest and the accompanying surface mass injection rates are also small for the cases analyzed here. However, the ablation process would keep the surface temperatures below the radiative-equilibrium wall values. The present results could change to large surface ablation values because of large radiative heating rates if a lower altitude is used for the aerobraking and/or the body size is increased. A parametric study would, therefore, be appropriate to evaluate these effects. Future results would also include cases when the gas composition adjacent to the surface is not 100% because of the ablation species.

The equilibrium chemistry results at a freestream velocity of 12 km/s and 70 km altitude are compared with the finite-rate chemistry calculations to characterize the nature of the flowfield chemistry. This comparison shows that the flowfield is in chemical equilibrium for this condition. Consequently, the assumption of chemical equilibrium appears appropriate for portions (peak heating) of the trajectories now under consideration.

## References

[1]National Commission on Space, *Pioneering the Space Frontier,* Bantam Books, New York, May 1986.

[2]Walberg, G. D., "A Survey of Aeroassisted Orbit Transfer," *Journal of Spacecraft and Rockets,* Vol. 22, No. 1, 1985, pp. 3–18.

[3]Walberg, G. D., "A Review of Aerobraking for Mars Missions," International Astronautical Federation Paper IAF-88-196, Oct. 1988.

[4]Wilson, K. H., "Stagnation Point Analysis of Coupled Viscous-Radiating Flow with Massive Blowing," NASA CR-1548, June 1970.

[5]Rigdon, W. S., Dirling, R. B., Jr., and Thomas, M., "Stagnation Point Heat Transfer During Hypervelocity Atmospheric Entry," NASA CR-1462, Feb. 1970.

[6]Esch, D. D., Pike, R. W., Engel, C. D., Farmer, R. C., and Balhoff, J. F., "Stagnation Region Heating of a Phenolic-Nylon Ablator During Return from Planetary Mission," NASA CR-112026, Sept. 1971.

[7]Garrett, L. B., Smith, G. L., and Perkins, J. N., "An Implicit Finite-Difference Solution to the Viscous Shock Layer Including the Effects of Radiation and Strong Blowing," NASA TR R-388, Nov. 1972.

[8]Sutton, K., "Characteristics of Coupled Nongray Radiating Gas Flows with Ablation Product Effects About Blunt Bodies During

Planetary Entries," Ph.D. Dissertation, North Carolina State Univ., Raleigh, NC, 1973; see also *AIAA Journal,* Vol. 12, No. 8, 1974, pp. 1099–1105.

[9]Moss, J. N., "Radiative Viscous-Shock-Layer Solutions with Coupled Ablation Injection," *AIAA Journal,* Vol. 14, No. 9, 1976, pp. 1311–1317.

[10]Moss, J. N., "Reacting Viscous Shock-Layer Solutions with Multicomponent Diffusion and Mass Injections," NASA TR R-411, June 1974.

[11]Moss, J. N., Zoby, E. V., and Sutton, K., "A Study of the Aerothermal Environment for the Pioneer Venus Multiprobe Mission," AIAA Paper 77-766, June 1977.

[12]Zoby, E. V., and Moss, J. N., "Preliminary Thermal Analysis for Saturn Entry," AIAA Paper 80-0359, Jan. 1980.

[13]Moss, J. N., and Simmonds, A. L., "Galileo Probe Forebody Flowfield Predictions," *Entry Vehicle Heating and Thermal Protection Systems: Space Shuttle, Solar Starprobe, Jupiter Galileo Probe,* edited by P. E. Bauer and H. E. Collicott, Vol. 85, Progress in Astronautics and Aeronautics, AIAA, New York, 1983, pp. 419–445.

[14]Park, C., and Milos, F. S., "Computational Equations for Radiating and Ablating Shock Layers," AIAA Paper 90-0356, Jan. 1990.

[15]Kumar, A., Tiwari, S. N., and Graves, R. A., Jr., "Radiating Viscous Shock Layer Solutions for Jovian Entry at Angle of Attack," *Outer Planet Entry Heating and Thermal Protection,* edited by R. Viskanta, Vol. 64, Progress in Astronautics and Aeronautics, AIAA, New York, 1979, pp. 147–164.

[16]Gupta, R. N., Lee, K. P., Moss, J. N., and Zoby, E. V., "Viscous Shock-Layer Analysis of Hypersonic Flows over Long Slender Bodies," *Journal of Spacecraft and Rockets,* Vol. 27, No. 2, 1990, pp. 174–184; see also AIAA Paper 87-2487, Aug. 1987.

[17]Lee, K. P., "Viscous Shock Layer Analysis of Hypersonic Flows Over Long Slender Vehicles," Ph.D. Dissertation, School of Engineering, Old Dominion Univ., Norfolk, VA, Aug. 1988.

[18]Nicolet, W. E., "Advanced Methods for Calculating Radiation Transport in Ablation-Product Contaminated Boundary Layers," NASA CR-1656, Sept. 1970.

[19]Nicolet, W. E., "User's Manual for the Generalized Radiation Transfer Code (RAD/EQUIL)," NASA CR-116353, Oct. 1969.

[20]Vincenti, W. G., and Kruger, C. H., Jr., *Introduction to Physical Gas Dynamics,* Wiley, New York, 1967, pp. 162–163.

[21]Shinn, J. L., "Optical Absorption of Carbon and Hydrocarbon Species from Shock Heated Acetylene and Methane in the 135-220 m Wavelength Range," *Thermophysics of Atmospheric Entry,* edited by T. E. Horton, Vol. 82, Progress in Astronautics and Aeronautics, AIAA, New York, 1982, pp. 68–80.

[22]Stroud, C. W., and Brinkley, K. L., "Chemical Equilibrium of Ablation Materials Including Condensed Species," NASA TN D-5391, Aug. 1969.

[23]Gupta, R. N., Yos, J. M., Thompson, R. A., and Lee, K. P., "A Review of Reaction Rates and Thermodynamic and Transport Properties for an Eleven-Species Air Model for Chemical and Thermal Nonequilibrium Calculations to 3000 K," NASA RP-1232, Aug. 1990.

[24]Gupta, R. N., Lee, K. P., Moss, J. N., and Sutton, K., "Viscous-Shock-Layer Solutions with Coupled Radiation and Ablation Injection for Earth Entry," AIAA Paper 90-1697, June 1990.

[25]Browne, W. G., "Thermodynamic Properties of Some Atoms and Atomic Ions," Missile and Space Vehicle Dept., Engineering Physics, TM2, General Electric Co., Valley Forge, PA, 1962.

[26]Browne, W. G., "Thermodynamic Properties of Some Diatoms and Diatomic Ions," Missile and Space Vehicle Dept., Engineering Physics, TM8, General Electric Co., Valley Forge, PA, 1962.

[27]JANNAF Thermochemical Tables, 3rd ed., Pts. I and II, Dow Chemical U.S.S., Midland, MI, 1985.

[28]McBride, B. J., Heimel, S., Ehlers, J. G., and Gordon, S., "Thermodynamic Properties to 6000 K for 210 Substances Involving the First 18 Elements," NASA SP-3001, March 1963.

[29]Bahn, G. S., "Approximate Thermochemical Tables for Some C-H and C-H-O Species," NASA CR-2178, March 1973.

[30]Hirschfelder, J. O., Curtiss, C. F., and Bird, R. B., *Molecular Theory of Gases and Liquids,* Wiley, New York, 1967.

[31]Svehla, R. A., "Estimated Viscosities and Thermal Conductivities of Gases at High Temperatures," NASA TR R-132, April 1962.

[32]Yos, J. M., private communication, 1985.

[33]Armaly, B. F., and Sutton, K., "Viscosity of Multicomponent Partially Ionized Gas Mixtures," AIAA Paper 80-1495, July 1980.

[34]Mason, E. A., and Saxena, S. C., "Approximation Formula for the Thermal Conductivity of Gas Mixtures," *Physics of Fluids,* Vol. 1, No. 5, 1958, pp. 361–369.

[35]Engel, C. D., Farmer, R. C., and Pike, R. W., "Ablation and Radiation Coupled Viscous Hypersonic Shock Layers," NASA CR-112306, Sept. 1971.

[36]Esch, D. D., Siripong, A., and Pike, R. W., "Thermodynamic Properties in Polynomial Form for Carbon, Hydrogen, Nitrogen, and Oxygen Systems From 500 to 15000 K," NASA CR-111989, Nov. 1970.

[37]Swann, R. T., "Approximate Analysis of the Performance of Char-Forming Ablators," NASA TR R-195, June 1964.

[38]Dow, M. B., and Swann, R. T., "Determination of Effects of Oxidation on Performance of Charring Ablators," NASA TR R-196, June 1964.

[39]Hill, O., "Manned Mars Mission Vehicle Design Requirements for Aerocapture," Manned Mars Mission Conference, NASA TM 89320 (or NASA M002), June 1986.

James E. Daywitt
*Associate Editor*